

Electronic Supplementary Information

Single-phase Ni₅P₄-Copper foam superhydrophilic and aerophobic core-shell nanostructures for efficient hydrogen evolution reaction

Manisha Das, Nityasagar Jena, Taniya Purkait, Navpreet Kamboj, Abir De Sarkar and

*Ramendra Sundar Dey**

Institute of Nano Science and Technology, Phase - 10, Sector - 64, Mohali, Punjab
160062, India.

*Corresponding Author E-mail: rsdey@inst.ac.in

Experimental sections

Materials. Nickel chloride ($\text{NiCl}_2 \cdot 6\text{H}_2\text{O}$), sodium dihydrogen phosphate ($\text{NaH}_2\text{PO}_4 \cdot \text{H}_2\text{O}$), sulphuric acid (H_2SO_4), nitric acid (HNO_3), copper sulphate ($\text{CuSO}_4 \cdot 5\text{H}_2\text{O}$), sodium hypophosphite ($\text{NaH}_2\text{PO}_2 \cdot \text{H}_2\text{O}$), nickel foam, graphite plate platinum on carbon (Pt/C) and were purchased from Sigma Aldrich. A high-purity copper foil was purchased from Gelon LIB group, China (Thickness-1-5 μm). All other chemicals used were of analytical grade and used as received.

Physical Characterizations. All the electrochemical measurements such as cycling voltammetry (CV), Chronopotentiometry (CP) and linear sweep voltammetry (LSV) were carried out with CHI 760E electrochemical workstation. Electrochemical impedance spectroscopy (EIS) was performed with of Metrohm Autolab (M204 multichannel potentiostat galvanostat) attached with FRA 32M module. Powder X-ray diffraction (PXRD) pattern was obtained on a Bruker D8 Advances instrument using $\text{Cu-K}\alpha$ ($\lambda = 1.5406 \text{ \AA}$) radiation in the 2θ range from 10° to 80° with an acceleration voltage of 40KV. Scanning Electron Microscopy (SEM) JeolJSMIT300 equipped with a BrukerXFlash 6130 integrated with Energy Dispersive X-ray Spectroscopy (EDS) to investigate the surface morphology and the elemental composition of the as synthesized material. Transmission Electron Microscopy (TEM), High-Resolution TEM (HRTEM), Selected Area Electron Diffraction (SAED) and Elemental mapping studies were performed with a JEM2100. X-ray photoelectron spectroscopy (XPS) was collected in an ultrahigh vacuum chamber (2×10^{-9} mbar) using (Monochromatic) with 6 mA beam current by $\text{K}\alpha$ plus XPS system by ThermoFisher Scientific instruments (UK). Nitrogen adsorption-desorption analysis was done at 77 K on an Autosorb iQ2 instrumental setup to examine the surface area by Brunauer Emmett Teller (BET) method. The pore size distribution analysis of the sample was carried out with the Barrett, Joyner

& Halenda (BJH) method. Hydrophilic nature of the catalyst was analyzed with the help of drop size analyzer, KRUSS (DSA25E, 100 watt).

Computational details:

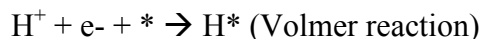
In geometry optimization using DFT, a constraint optimization was applied in order to reduce the enormous computational demand of the calculations. The surface atomic coordinates were allowed to relax fully, while 2-3 atomic layers below the surface layer were held at the initial positions corresponding to their bulk structure, using the selective dynamics option implemented within the Vienna *ab initio* simulation package (VASP)¹. In all cases, a spin-polarized DFT calculation were performed with conjugate gradient algorithm for the geometry optimization. The van der Waals' (vdW) dispersive interactions was performed within the DFT-D2 with a scaling parameter of 0.75 (VDW_SCALING = 0.75) and vdW radius of 30.0 (VDW_RADIUS = 30.0) with VDW_D = 20.0 in the VASP INCAR settings. The DFT harmonic vibrational frequencies for the zero-point energy (ZPE) and entropy, S calculation was calculated using a finite displacement method (IBRION = 5) where the intrinsic VASP symmetry flag (ISYM) was set to zero in order to avoid errors, which could possibly arise from any incorrect rendering of thermochemical energies with same settings for the vdW-DFT-D2 and energy threshold as used for the geometry relaxation.

Surface geometries for H-adsorption:

In order to build a Ni₅P₄ (0001) slab geometry, the bulk crystal of Ni₅P₄ in its P63mc (186) space group symmetry was optimized first. Upon geometry optimization, the lattice constants converged to a = b = 6.793 Å, c = 10.983 Å, which is in very close agreement with our PXRD analysis (a = b = 6.789 Å, c = 10.986 Å).

Mechanism for hydrogen evolution reaction

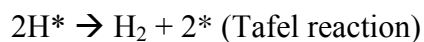
HER undergoes a multistep reaction process under acidic conditions, which is suggested as two different processes with three possible reactions. The first step is the discharge process, which is known as the Volmer reaction. In this particular step, an electron is transferred to the surface of the cathode to capture a proton from the electrolyte, which forms an intermediate state of an adsorbed hydrogen atom on the catalytic surface active site:



The generation of H_2 follows two different ways, Heyrovsky reaction and Tafel reaction. With low H^* coverage, the generation of H_2 takes place when the adsorbed hydrogen atom couple with an electron and another proton in the electrolyte. This electrochemical desorption step is termed Heyrovsky reaction:



However, with a relatively high H^* coverage, the combination between the adjacent adsorbed hydrogen atoms is predominant, which is known as Tafel reaction, also called the chemical desorption step:



Tafel plot

The linear region of the plots were fitted using the Tafel formula

$$Z = b \cdot \log(j) + a,$$

where 'Z' refers to overpotential, 'j' refers to current density, 'a' is the exchange current density and 'b' refers to the Tafel slope.

Electrochemically Active Surface Area (ECSA) and roughness factor (RF)

The surface roughness factor (RF) of $\text{Cu}@Ni_5P_4$ electrodes was estimated by measuring its electrochemically active surface area (ECSA) from its electrochemical doublelayer capacitance

(C_{dl}). Cyclic voltammetry (CV) scans of the electrodes in a non-Faradaic region 0.5M H₂SO₄ electrolyte at different scan rates (25 to 200 mV/s) is shown in Figure S10a and S10b, respectively. The potential windows were restricted to a non-faradic region. The double-layer charging current is equal to the product of the scan rate, v , and the electrochemical double-layer capacitance, C_{dl} , as given by equation,

$$i_c = vC_{dl}$$

The difference in the fitted slopes of forward and backward CV scans was used to determine the C_{dl} , which is 33.9 mF cm⁻².² ECSA is then calculated by dividing the C_{dl} by the specific surface capacitance (C_{sp}) of electrode surface as follows:

$$ECSA = C_{dl}/C_{sp}$$

The roughness factor was calculated by using formula³

$$RF (\text{catalyst}) = \text{catalyst active surface area substrate}/\text{geometric surface area}$$

A commonly used C_{sp} value of nickel surfaces 20 $\mu\text{F}/\text{cm}^2$ was used for 0.5M H₂SO₄ electrolyte⁴. ECSA of 423.5 cm² and a roughness factor 1694 was calculated for as prepared Cuf@Ni₅P₄ electrode.

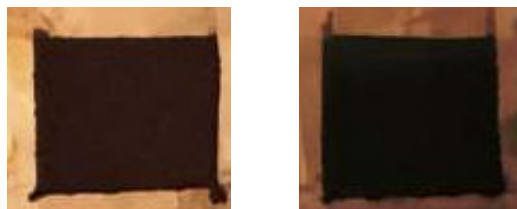


Figure S1. Digital photographs of electrodes (a) bare copper foam (b) Cuf@Ni₅P₄. The deposited electrode area is about $0.5 \times 0.5 \text{ cm}^2$.

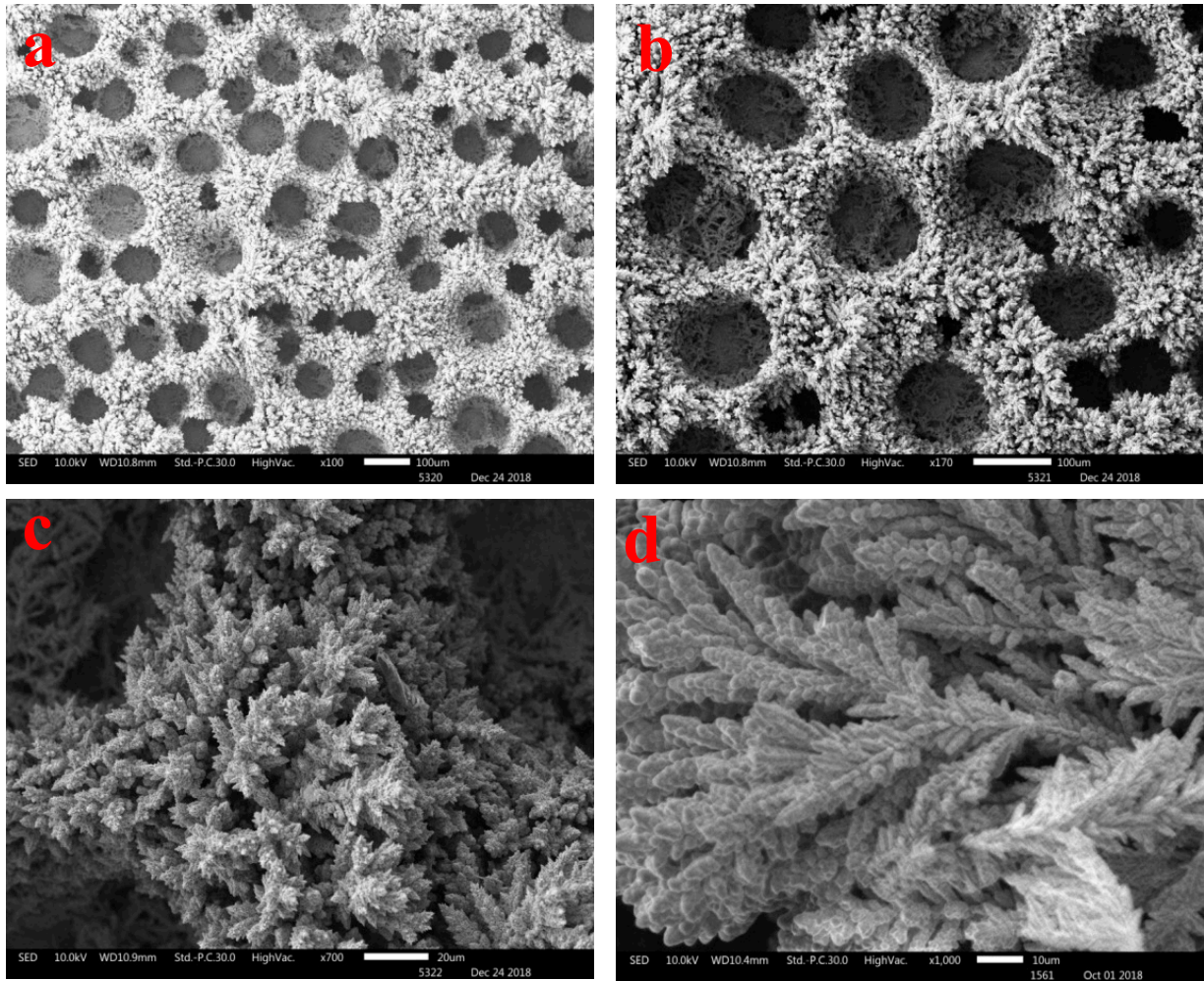


Figure S2. SEM images of bare CuF at different magnification (a-b) 100 μ m (c) 20 μ m (d) 10 μ m

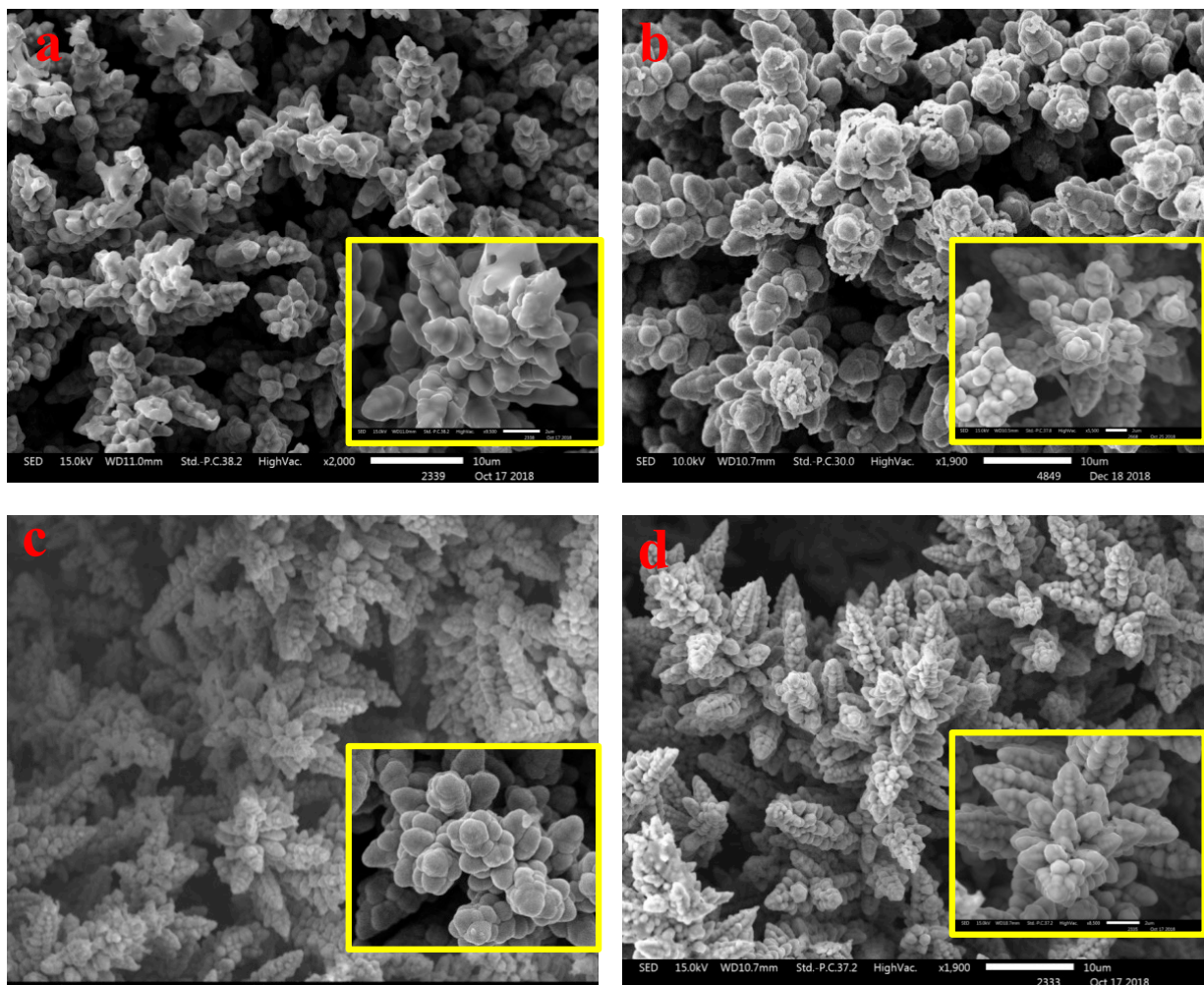


Figure S3. SEM images of electrodeposited samples at different time (a) 30 min (b) 60 min (c) 90 min (d) 120 min

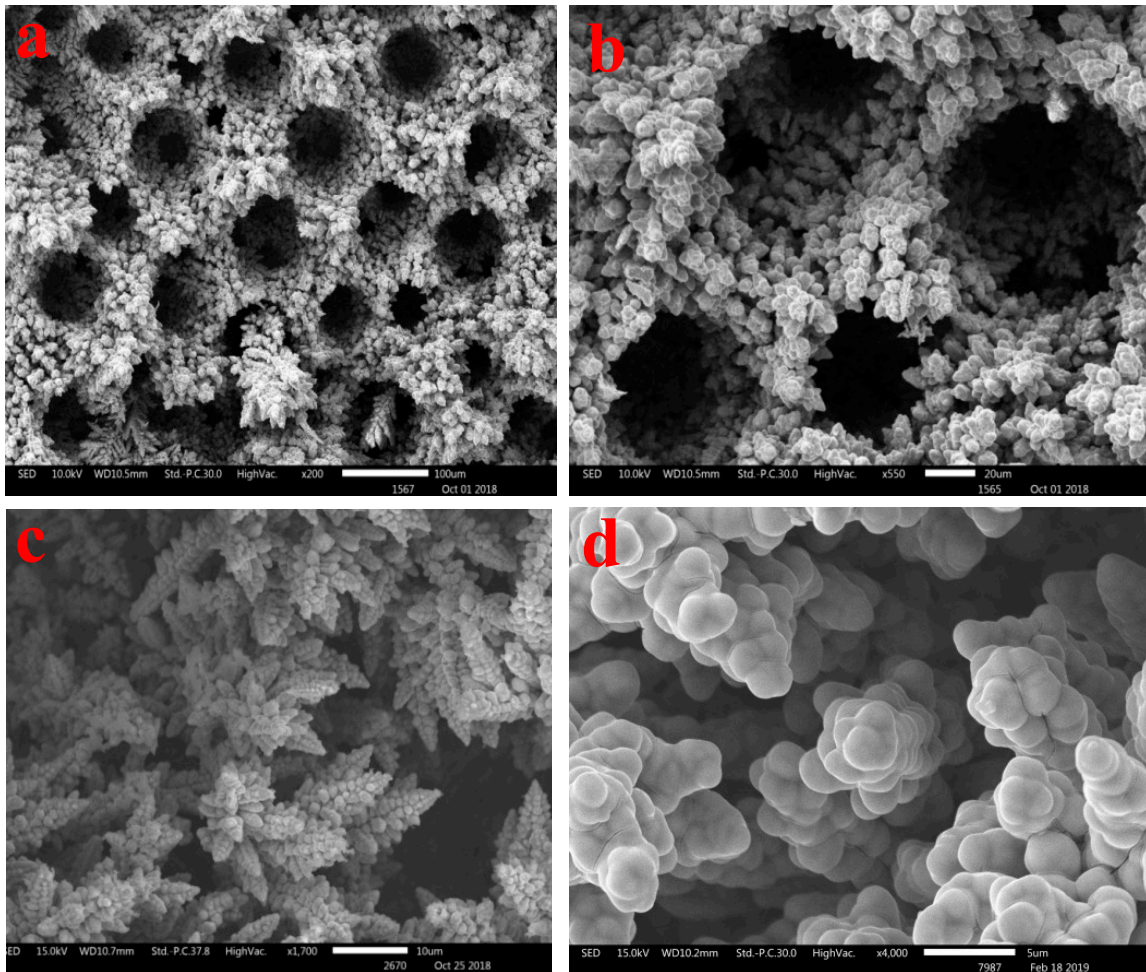


Figure S4. SEM images of Cuf@Ni₅P₄ at different magnifications (a) 100 μm (b) 20 μm (c) 10 μm (d) 5 μm

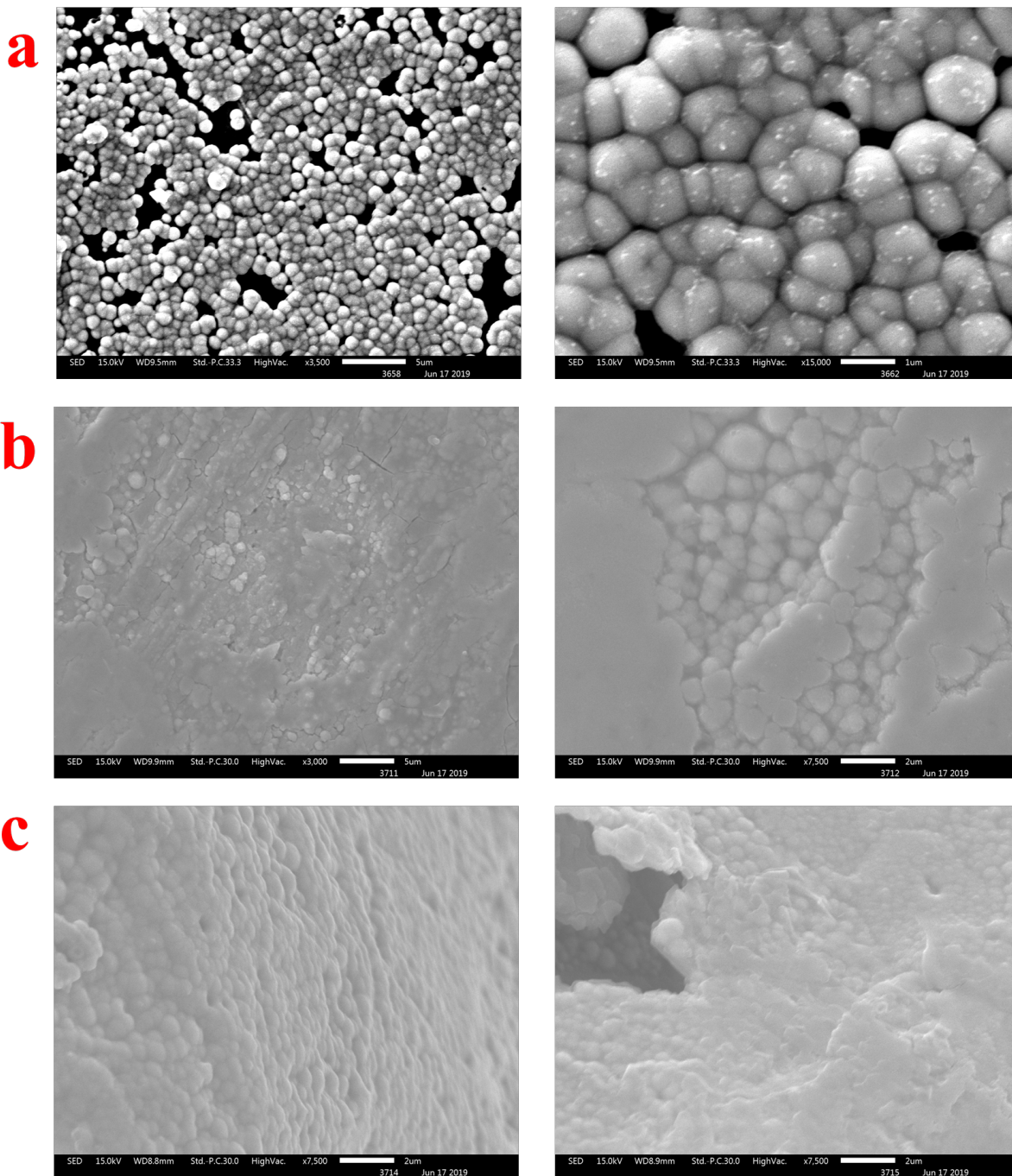


Figure S5. SEM images of Ni_5P_4 on different substrates (a) $\text{Ni}_5\text{P}_4/\text{GP}$ (b) $\text{Ni}_5\text{P}_4/\text{Cu}$ foil (c) $\text{Ni}_5\text{P}_4/\text{Nif}$

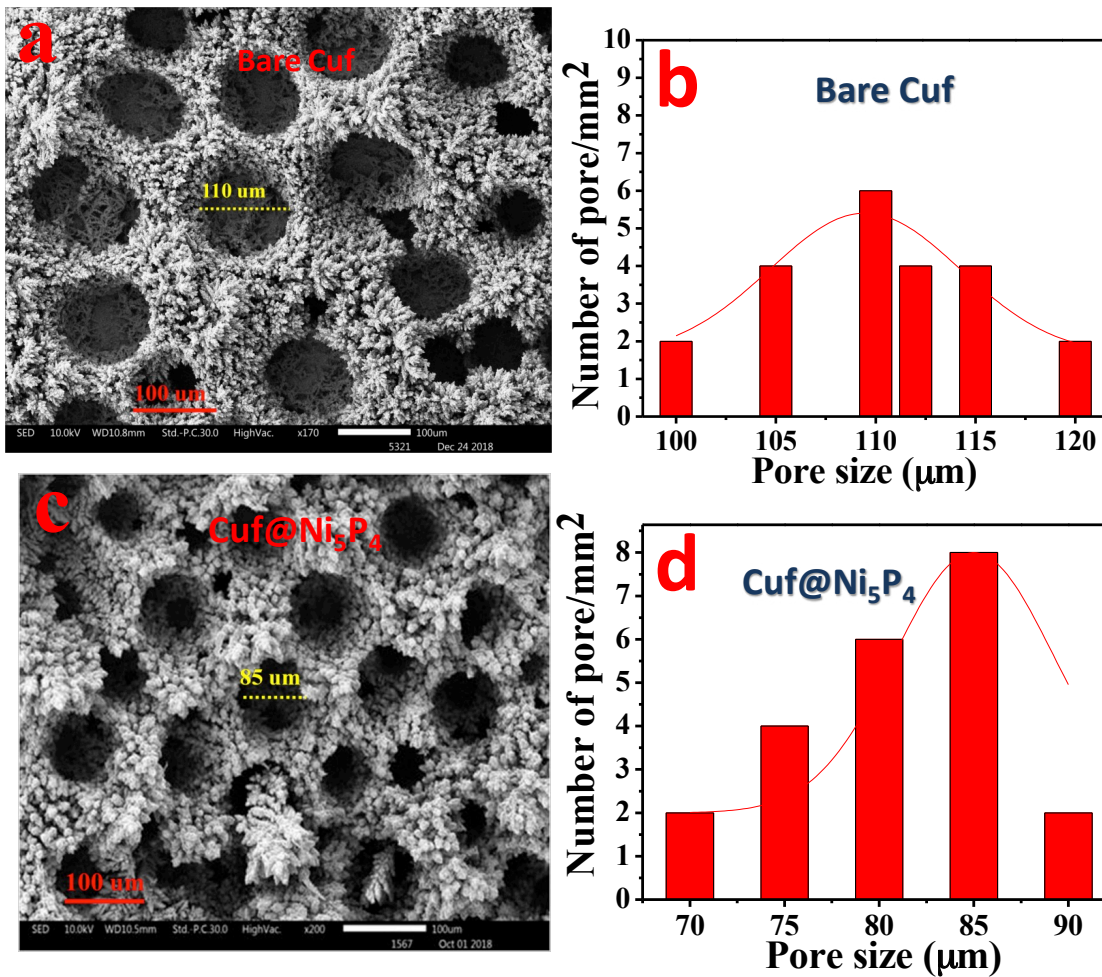


Figure S6. (a) SEM image of bare copper foam at a magnification of 100 μm (b) Average pore size distribution of bare CuF (c) SEM image of CuF@Ni₅P₄ at a magnification of 100 μm (d) Average pore size distribution of CuF@Ni₅P₄

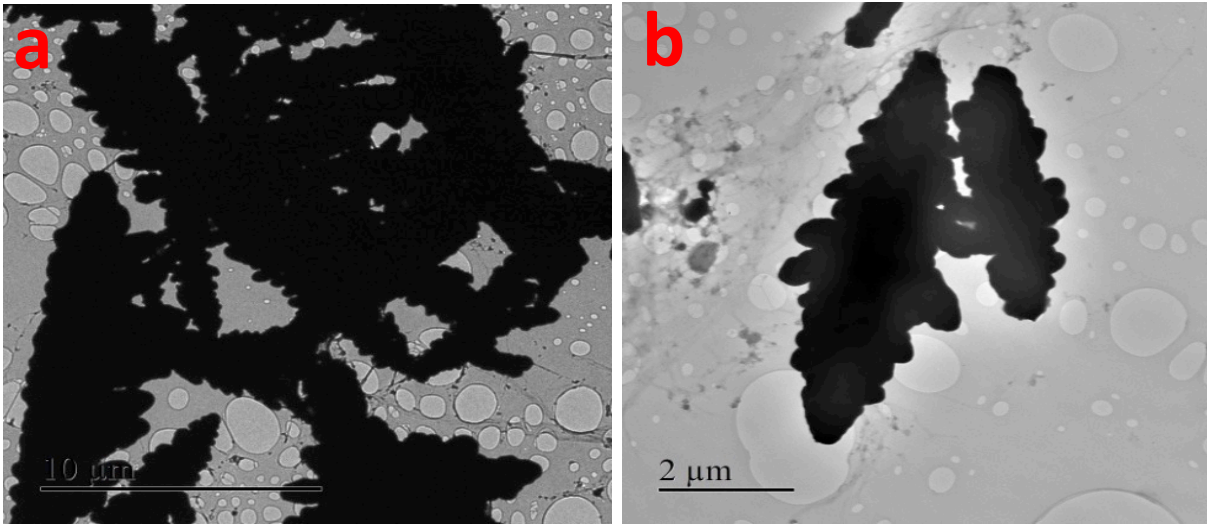


Figure S7. TEM images of Cuf@Ni₅P₄ at different magnifications Scale bar: (a) 10 μm (b) 2 μm.

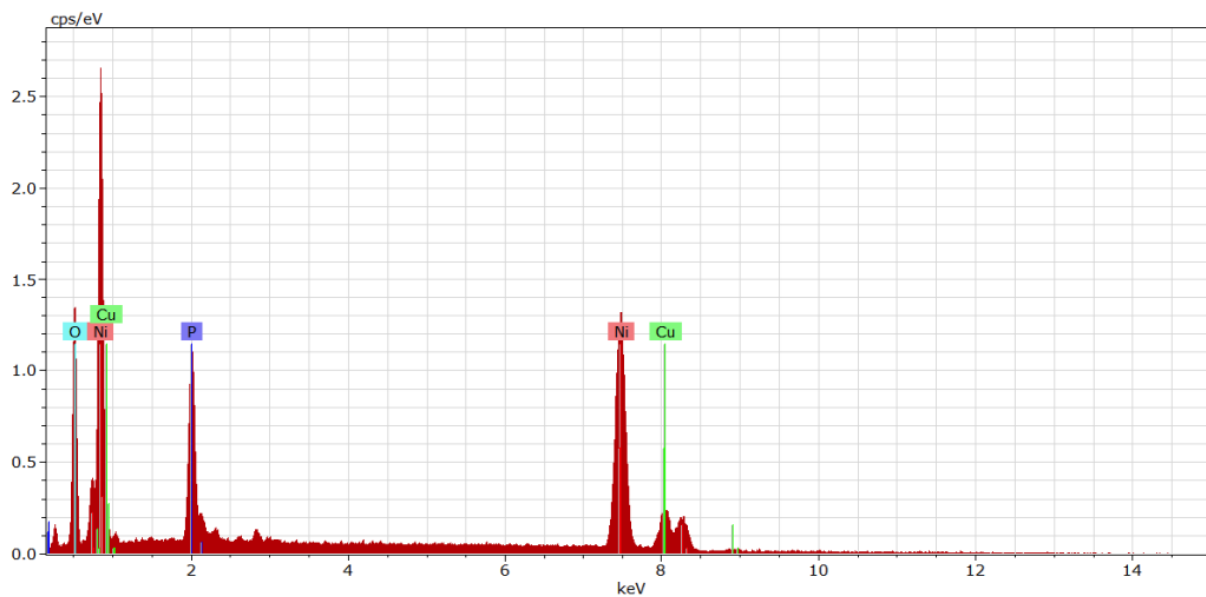


Figure S8. EDX image of Cuf@Ni₅P₄

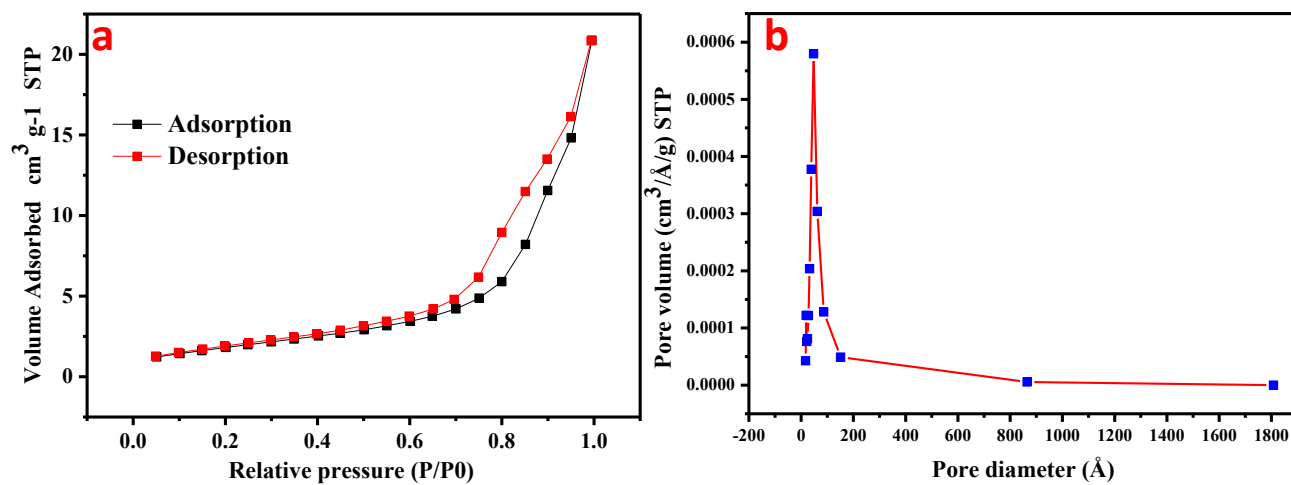


Figure S9. (a) Nitrogen adsorption-desorption isotherm and (b) corresponding BJH pore size distributions of Cu@Ni₅P₄

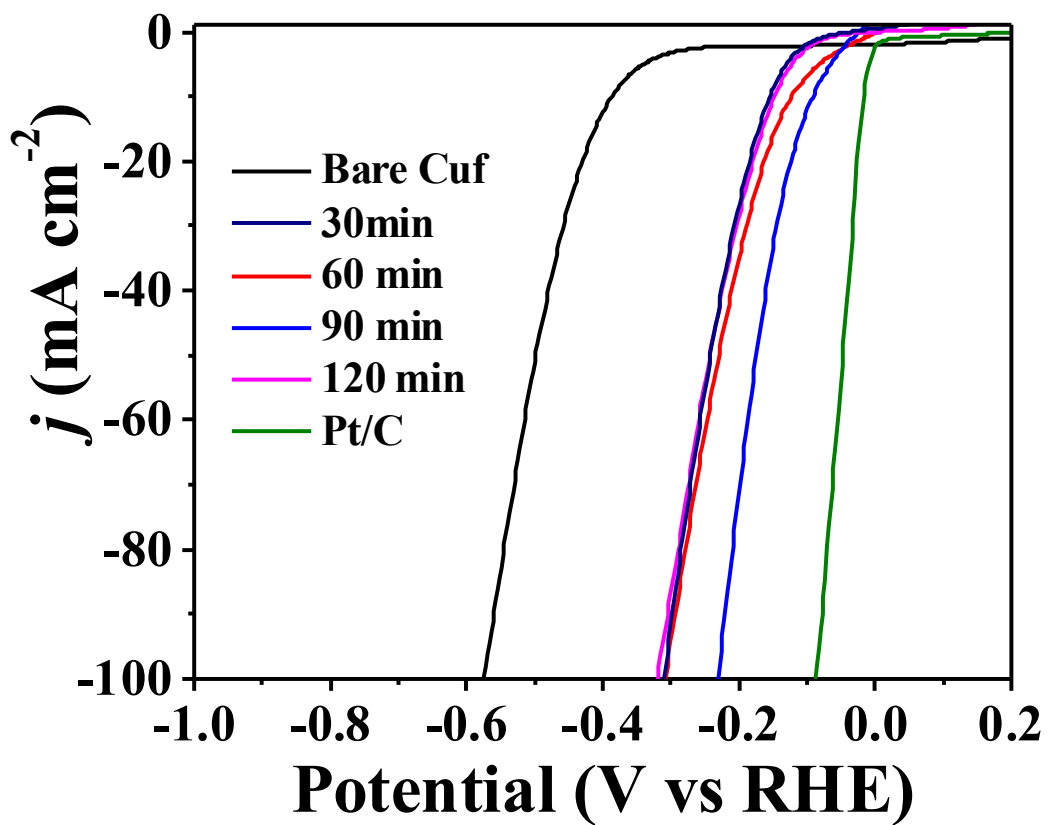


Figure S10. Linear sweep voltammetry of as prepared catalyst for different deposition time at a potential of -0.2 V vs RHE

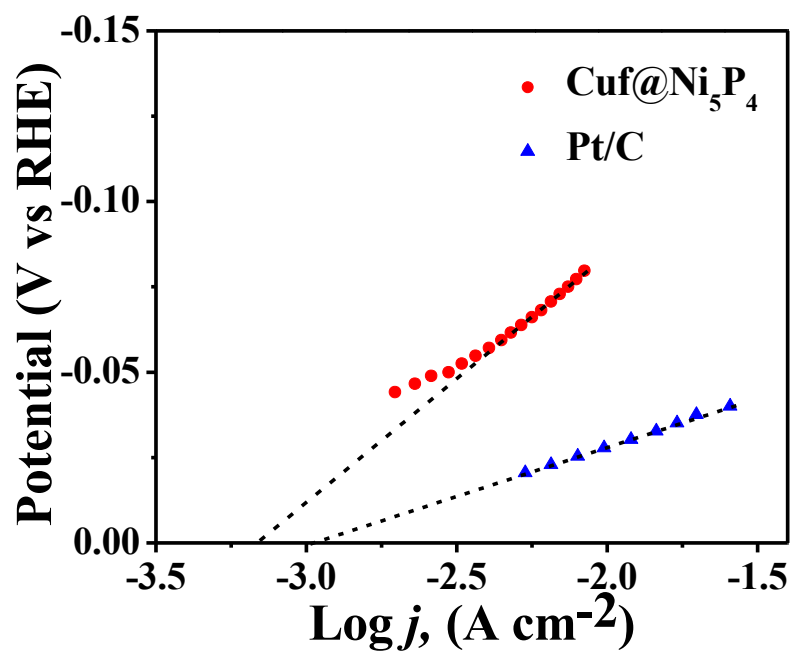


Figure S11. Calculated exchange current densities of Pt/C and Cuf@Ni₅P₄ by applying extrapolation method to the tafel plots.

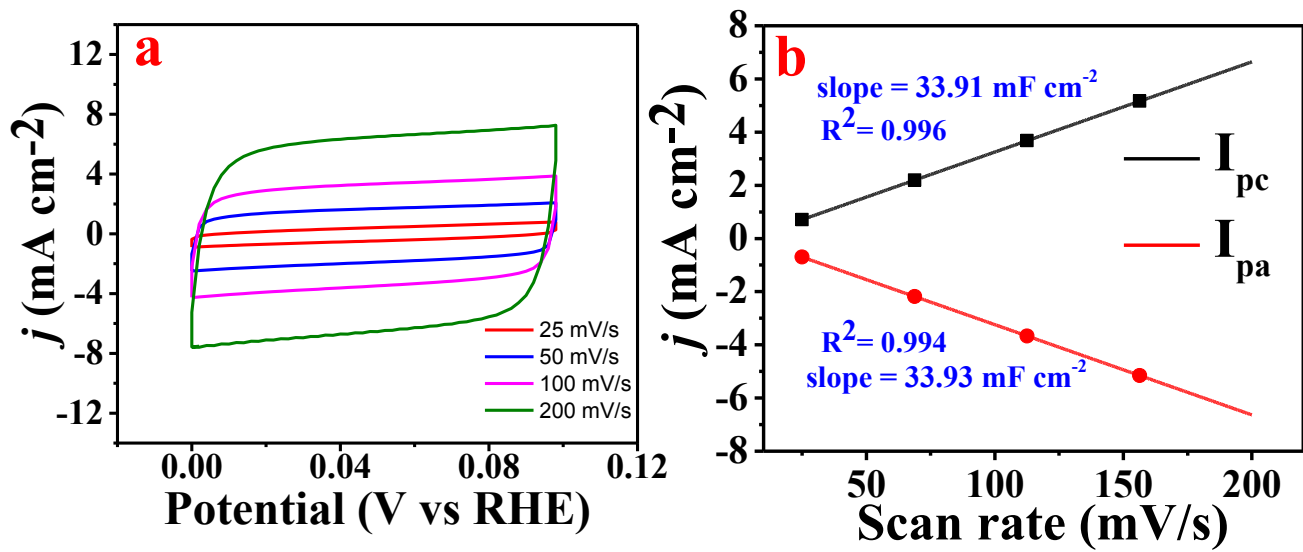


Figure S12. (a) CV scans of Cuf@Ni₅P₄ in a non-Faradic region at different scan rates (b) Linear fits of current densities at different scan rates

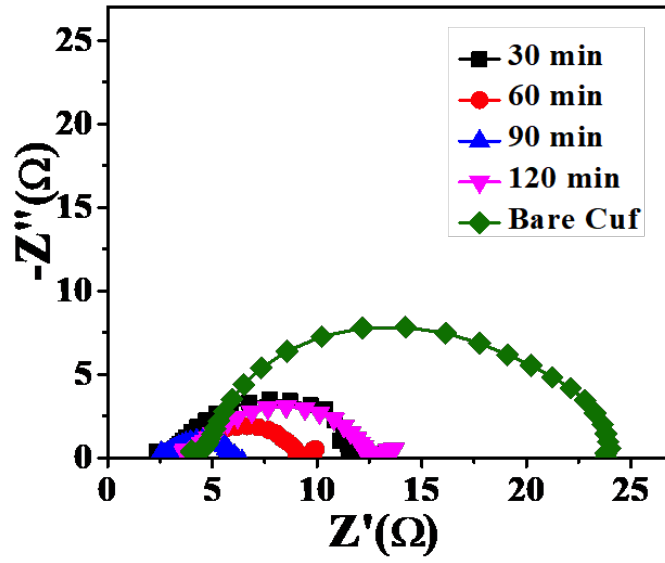


Figure S13. Electrochemical impedance spectroscopy of as prepared catalyst for different deposition time at a potential of -0.2 V vs RHE

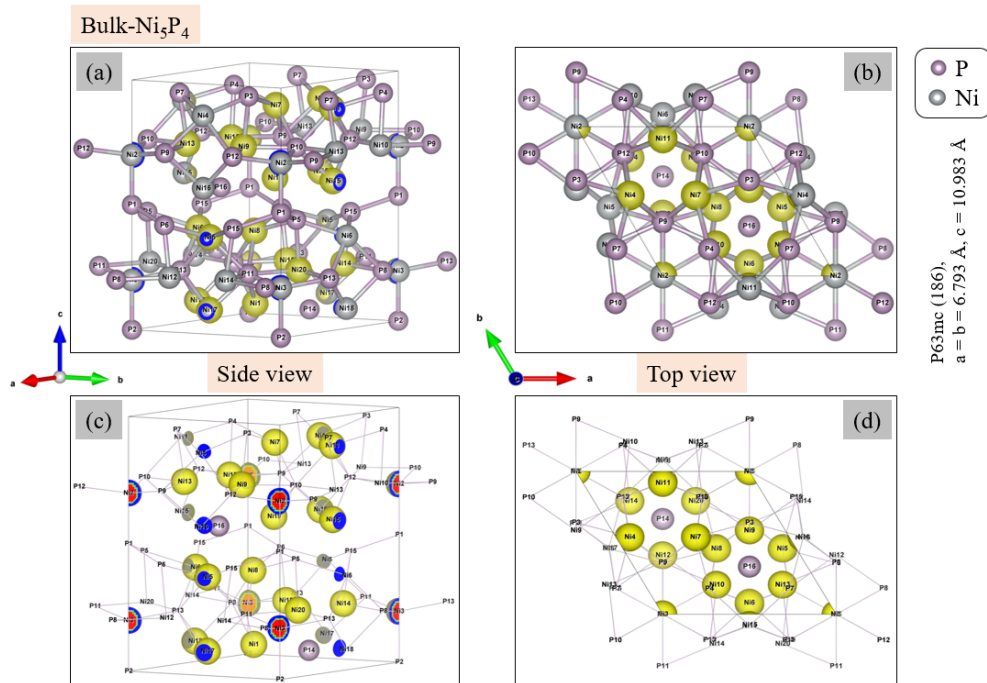


Figure S14. Bulk optimized geometry of Ni₅P₄ crystal with ground state charge density distribution around Ni, P atomic sites. The charge density isosurfaces is presented at an isolevel of $0.46 \text{ e}/\text{\AA}^3$.

Figure S14, shows the top and side views of a bulk Ni₅P₄ crystal with ground state valence charge distribution around the Ni and P atomic sites. The charge density distribution is much higher around the Ni site than the P site as shown in Figure S14 (c-d).

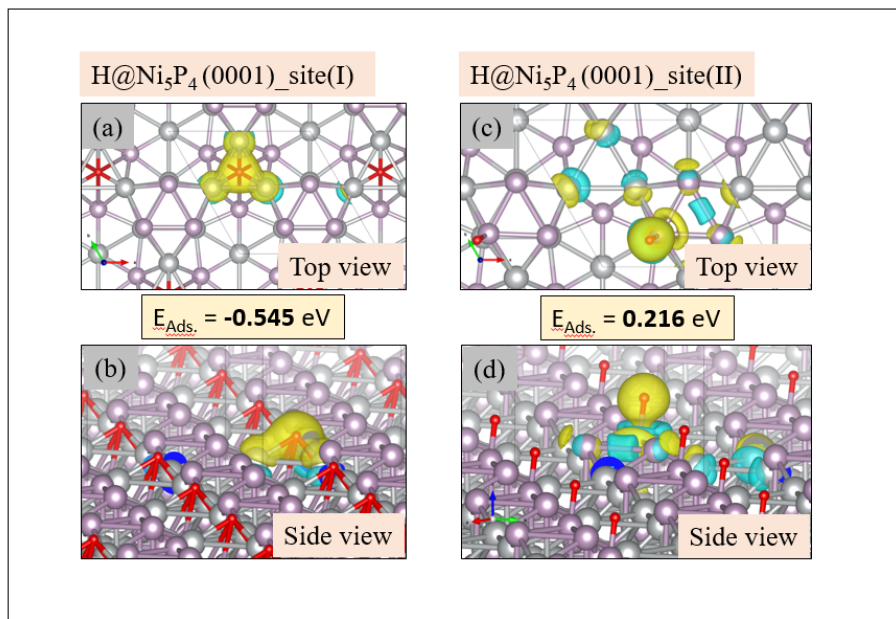


Figure S15. A top and side view representation of Ni_5P_4 (0001) surface with hydrogen (H) adsorption over the 3-fold Ni site (a-b), and (c-d) on-top P site of Ni_5P_4 (0001). The differential charge density distribution is at an isolevel of $0.85 \times 10^{-2} \text{ e}/\text{\AA}^3$ with hydrogen adsorption energy ($E_{\text{Ads.}}$) -0.54 eV for H-adsorbed over the 3-fold Ni site and 0.21 eV at the on-top P site.

We build a slab model of Ni_5P_4 along the hexagonal (0001) direction from the bulk-optimized geometry of Ni_5P_4 . The slab model of Ni_5P_4 (0001) consists of 3-atomic layers along the (0001) axis using a coordinated geometry of Ni, P atoms as the surface atomic layer where the P atoms is at the top surface and Ni atoms slightly beneath the P layer, under surface optimization.

We computationally screened several hydrogen adsorption sites around the Ni and P atoms. As shown in Figure S15, the 3-fold Ni site and on-top P site turns out to be the most preferable H-adsorption site with binding energy -0.54 eV and 0.21 eV, respectively.

The hydrogen adsorption energy ($E_{\text{Ads.}}$) is the ground state energy difference between the H-adsorbed surface ($E_{\text{surface+H}}$) to that of adsorption free surface (E_{surface}) w.r.t the energy of H_2 molecule in the gas phase.

$$E_{\text{Ads.}} = E_{\text{surface+H}} - E_{\text{surface}} - \frac{1}{2} E_{\text{H}_2}$$

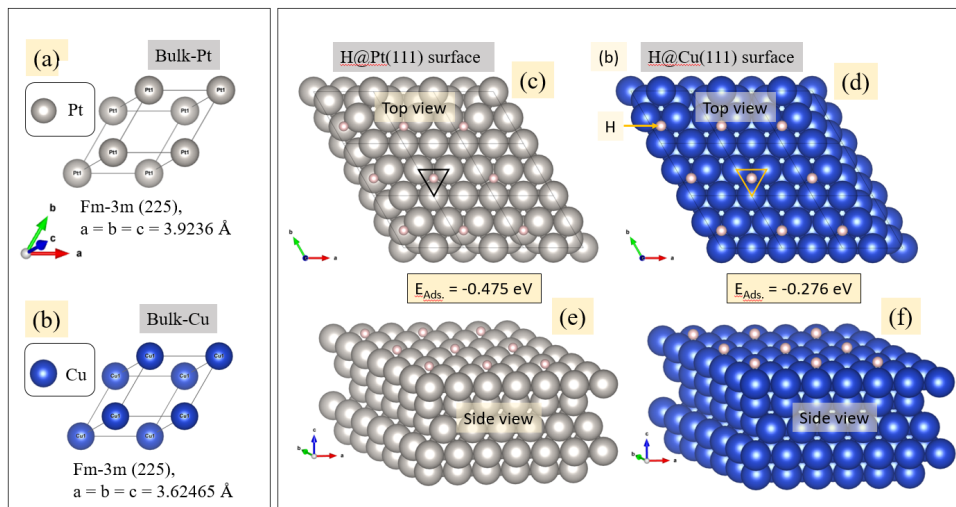
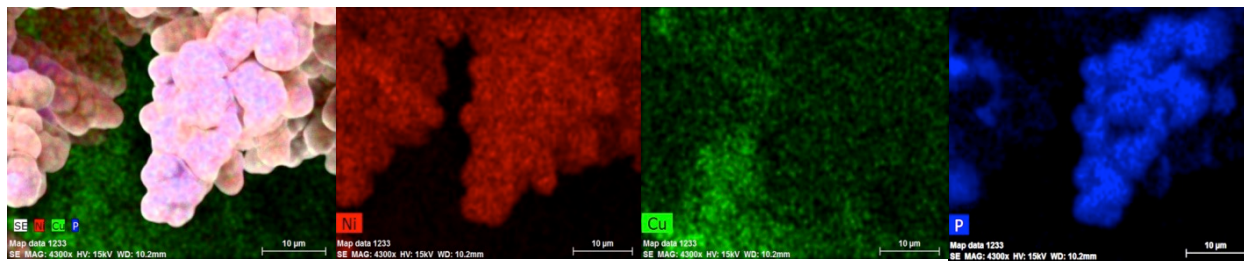


Figure S16. Hydrogen adsorption geometry on Pt (111) and Cu (111) surface.

In order to create a Ni₅P₄ (0001)/Cu(111) hydride interface geometry, a 5 atomic layer of Cu (111) surface have been optimized from its bulk optimized crystal as shown in Figure S16 where top 2 Cu layer has been fully relaxed by keeping bottom 3 Cu layers to its bulk lattice constants. A similar surface geometry has been considered for the Pt (111) surface with H-adsorption over the 3-fold Cu site and 3-fold Pt site as shown in figure (c-f). For Pt (111) surface the H-adsorption energy is found to be smaller which is -0.47 eV than the Cu (111) surface, -0.27 eV.

a Before stability



b After stability

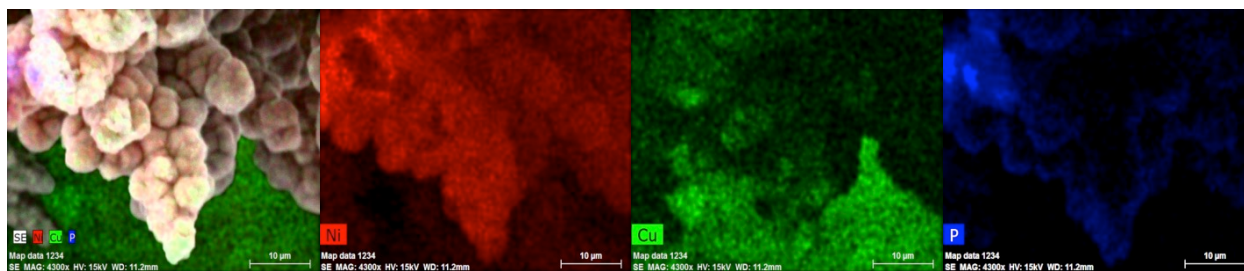


Figure S17. Elemental mapping of Cuf@Ni₅P₄ obtained (a) before and (b) after 84 hrs chronopotentiometry test.

Table S1. HER performance comparison between $\text{Cu}@Ni_5P_4$ and recently reported catalyst in 0.5M H_2SO_4

Catalyst	Electrolyte	Overpotential 1 (mV)@10 mA cm^{-2}	Overpotential (mV)100 mA cm^{-2}	Tafel slope (mV/dec)	References
Ni_5P_4	1 M H_2SO_4	24	-	27	5
Ni_5P_4 on Nickel foil	0.5 H_2SO_4	140	-	46	6
Ni_5P_4 - Ni_2P NS array/ Ni Foam	0.5 M H_2SO_4	120	200	79.1	7
Ni_2P / Ti foil	0.5 M H_2SO_4	-	180	46	8
Ni_2P -G@NF/ Graphene/Ni foam	0.5 M H_2SO_4	55	170	30	9
NiP_2 NS/ carbon cloth	0.5 M H_2SO_4	75	204	51	10
Ni_{12}P_5 hollow spheres/ Glass carbon	0.5 M H_2SO_4	144	277	46	11
Ni_2P NRs/Ni/NF	0.5 M H_2SO_4	131	300	106.1	12
Ni_{12}P_5 /Ti	0.5 M H_2SO_4	107	-	63	13
Ni_2P /Ni foam	0.5 M H_2SO_4	-120	-	68	13
NiCoP /CC	0.5M H_2SO_4	48	137	-	14
NiP_2 NW/NF	0.5 M H_2SO_4	67	-	109	15
Ni_{12}P_5 Ni_2P /NF	0.5 M H_2SO_4	73	-	70.8	16
CP@Ni-P	0.5 M H_2SO_4	-	164	58.8	17
Ternary $\text{Ni}_{2x}\text{Co}_x\text{P}$	0.5 M H_2SO_4	59	-	50	18
Ni_xP_y	0.5 M H_2SO_4	62@20	-	46.1	19
NiCoP NPs	0.5 M H_2SO_4	96	148	68	18
Co/ Co_2P /NF	0.5 M H_2SO_4	186	-	156	20
$\text{Cu}@Ni_5P_4$	0.5 M H_2SO_4	90	164	49	This work

NS-nanosheet, NF-nickel foam, CC-carbon cloth, NR-nanorod, NW-nanowire, CP-carbon fiber paper, NP-nanoparticle.

Table S2. Comparison of Exchange current density between Cuf@Ni₅P₄ and recently reported catalyst.

Catalyst	Onset potential (mV)	Overpotential mV@mAcm ⁻²	Tafel slope	Exchange current density (A/cm ²)	References
Ni ₁₂ P ₅ / GCE	380	-	270	4.5x10 ⁻⁵	20
Ni ₁₂ P ₅ / GCE	80	208@10	75	2.857x10 ⁻⁵	21
Ni ₂ P/ GCE	62	137@10	49	4.592x10 ⁻⁵	21
Ni ₅ P ₄ / GCE	34	118@10	42	5.702x10 ⁻⁵	21
Ni ₂ P/ Ti foil		130@20	46	3.3x10 ⁻⁵	8
Ni ₂ P/ GCE	75	172@10	62	7.1x10 ⁻⁵	22
Cuf@ Ni₅P₄	54	90@10	49	76x10⁻⁵	This work

Table S3. Thermochemical energies of reaction intermediate (H*) over different metal surfaces and zero-point energy of H₂ molecule in gas-phase state at standard condition.

H* on metal-surface	E _{ZPE} (eV)	Entropy, S (eV/K)	ΔG _{H*} (eV)
Pt(111)	0.287	0.00370	-0.26043
Cu(111)	0.381	0.00302	0.03261
Ni ₅ P ₄ (0001)_3-fold_Ni (site I)	0.430	0.00168	-0.18728
Ni ₅ P ₄ (0001)_on-top_P (site II)	0.451	0.00171	0.59461
Ni ₅ P ₄ (0001)/Cu(111)_3-fold_Ni (site I)	0.345	0.00126	-0.52339
Ni ₅ P ₄ (0001)/Cu(111)_on-top_P (site II)	0.372	0.00131	0.46225
H ₂ (gas phase)	0.275	--	--

Table S3 summarize the zero-point energy (E_{ZPE}), entropy (S) and Gibbs' free energy change of HER reaction intermediate (H*) on different metal-catalyst surface.

References

- 1 G. Kresse and J. Furthmüller, *Phys. Rev. B*, 1996, **54**, 11169–11186.
- 2 C. Fisica and U. Milano, *Pure Appl. Chem.*, 1991, **63**, 711–734.
- 3 J. D. Benck, Z. Chen, L. Y. Kuritzky, A. J. Forman and T. F. Jaramillo, 2012, 2–9.
- 4 C. C. L. McCrory, S. Jung, J. C. Peters and T. F. Jaramillo, *J. Am. Chem. Soc.*, 2013, **135**, 16977–16987.
- 5 A. B. Laursen, K. R. Patraju, M. J. Whitaker, M. Retuerto, T. Sarkar, N. Yao, K. V. Ramanujachary, M. Greenblatt and G. C. Dismukes, *Energy Environ. Sci.*, 2015, **8**, 1027–1034.
- 6 M. Ledendecker, S. K. Calderón, C. Papp, H. Steinrück, M. Antonietti and M. Shalom, 2015, 12538–12542.
- 7 X. Wang, Y. V. Kolen'Ko, X. Q. Bao, K. Kovnir and L. Liu, *Angew. Chemie - Int. Ed.*, 2015, **54**, 8188–8192.
- 8 E. J. Popczun, J. R. McKone, C. G. Read, A. J. Biacchi, A. M. Wiltrout, N. S. Lewis and R. E. Schaak, *J. Am. Chem. Soc.*, 2013, **135**, 9267–9270.
- 9 A. Han, S. Jin, H. Chen, H. Ji, Z. Sun and P. Du, *J. Mater. Chem. A*, 2015, **3**, 1941–1946.
- 10 P. Jiang, Q. Liu and X. Sun, 2014, 13440–13445.
- 11 J. Chang, S. Li, G. Li, J. Ge, C. Liu and W. Xing, *J. Mater. Chem. A Mater. energy Sustain.*, 2016, **4**, 9755–9759.
- 12 X. Wang, Y. V Kolen and L. Liu, *Chem. Commun.*, 2015, **1**, 3–6.
- 13 Y. Shi, Y. Xu, S. Zhuo, J. Zhang and B. Zhang, *ACS Appl. Mater. Interfaces*, 2015, **7**, 2376–2384.
- 14 C. Du, L. Yang, F. Yang, G. Cheng, W. Luo and M. Sciences, 1–15.

- 15 L. Wei, K. Goh, Ö. Birer, H. E. Karahan, J. Chang, S. Zhai, X. Chen and Y. Chen, *Nanoscale*, 2017, **9**, 4401–4408.
- 16 V. A. Online, Q. Lv, Z. Zhang and S. Wang, , DOI:10.1039/C6RA20737E.
- 17 X. Wang, W. Li, D. Xiong, D. Y. Petrovykh and L. Liu, *Adv. Funct. Mater.*, 2016, **26**, 4067–4077.
- 18 J. Li, M. Yan, X. Zhou, Z. Huang and Z. Xia, 2016, 1–12.
- 19 J. Li, J. Li, X. Zhou, Z. Xia, W. Gao, Y. Ma and Y. Qu, , DOI:10.1021/acsami.6b00731.
- 20 J. Masa, S. Barwe, C. Andronescu, I. Sinev, A. Ruff, K. Jayaramulu, K. Elumeeva, B. Konkena, B. R. Cuenya and W. Schuhmann, , DOI:10.1021/acsenergylett.6b00532.
- 21 Y. Pan, Y. Liu, J. Zhao, K. Yang, J. Liang, D. Liu, W. Hu, D. Liu, Y. Liu and C. Liu, *J. Mater. Chem. A*, 2015, **3**, 1656–1665.
- 22 T. Tian, L. Ai and J. Jiang, *RSC Adv.*, 2015, **5**, 10290–10295.